Wavefront measurement interferometry at the operational wavelength of extreme-ultraviolet lithography

Yucong Zhu,[1,*] Katsumi Sugisaki,[1] Masashi Okada,[1] Katsura Otaki,[1] Zhiqiang Liu,[1] Jun Kawakami,[1] Mikihiko Ishii,[1] Jun Saito,[1] Katsuhiko Murakami,[1] Masanobu Hasegawa,[2] Chidane Ouchi,[2] Seima Kato,[2] Takayuki Hasegawa,[2] Akiyoshi Suzuki,[2] Hideo Yokota,[2] and Masahito Niibe[3]

[1]EUVA Sagamihara R&D Center, 1-10-1 Asamizodai, Sagamihara, Kanagawa 228-0828, Japan
[2]EUVA Utsunomiya R&D Center, 23-10 Kiyohara-Kogyo-Danchi, Utsunomiya, Tochigi 321-3298, Japan
[3]University of Hyogo, 3-1-2 Kouto, Kamigori-cho, Ako-gun, Hyogo 678-1205, Japan

*Corresponding author: zhu.yucong@nikon.co.jp

Two basic types of interferometer, a point diffraction interferometer (PDI) and a lateral shearing interferometer (LSI) suitable for operation in the extreme-ultraviolet (EUV) wavelength region, are described. To address the challenges of wavefront measurement with an accuracy of 0.1 nm rms, we present a calibration method for the PDI that places a mask with two large windows at the image plane of the illumination point light source and a general approach to deriving the phase-shift algorithm series that eliminates the undesired zeroth-order effect in the LSI. These approaches to improving the measurement accuracy were experimentally verified by the wavefront measurements of a Schwarzschild-type EUV projection lens.   © 2007 Optical Society of America
  OCIS codes: 120.3940, 120.5050, 120.3180, 120.2650, 260.7200, 220.3740.

1. Introduction

By 2013, if we stay on the semiconductor industry's historic productivity curve, photolithography on wafers will be called for with critical feature sizes as small as 32 nm and below. Extreme-ultraviolet lithography (EUVL) tools will possibly help us achieve such critical dimension features and now is targeted to resolve minimum feature sizes of 32 nm and below. Among other potential next-generation lithography tools, EUVL preserves the experience and advantages of conventional optical lithography but produces high resolution due to its extremely short wavelength. However, since the light in the extreme-ultraviolet (EUV) wavelength region is not transmittable through most optical materials, it brings with it one of the largest difficulties in the manufacture of both projection lenses and its metrology system. In the final characterization of the wavefront aberrations of lithographic projection optics with all-reflective optical components, some research has shown potential uncertainty due to the response of the resonant–reflective multilayer coatings when tested at different wavelengths [1]. In this respect, wavefront characterization at the operational wavelength carries unambiguous performance information about the test optics. This becomes the key driver for developing EUV metrology. The typical wavelength of 13.5 nm is determined by the highest reflectivity one can get out of the Mo–Si multilayers coated on the surface of reflective components operated in the EUV wavelength region. In this paper, we provide descriptions of a point diffraction interferometer (PDI) and a lateral shearing interferometer (LSI) applied to wavefront metrology for EUVL lithography. The projection optics is aligned with a resulting wavefront error of ~1 nm rms. Such a wavefront tolerance places extremely high demands on the at-wavelength interferometry to provide measurement accuracy of the order of less than 0.1 nm rms. To achieve such high measurement accuracy, interferometer calibration and noise-insensitive phase analysis are essential issues. We present a simple

and easy-to-handle calibration method for the PDI and a phase-shifting algorithm series for the LSI. We report our experimental wavefront measurement of a 0.2 NA Schwarzschild-type lithographic projection lens on both the PDI and the LSI to verify the calibration method and algorithm series proposed in this paper.

2. Descriptions of the Point Diffractive Interferometer and the Lateral Shearing Interferometer

A schematic diagram of the PDI used in our experiment is shown in Fig. 1(a). The test optics is illuminated with spatially coherent light that is diffracted at the first mask from a pinhole smaller than the diffraction-limited focused spot for a certain illumination numerical aperture, so that the aberration from the optical source is spatially filtered out by it. A second mask with a large window and a small pinhole is placed at the image plane of the tested optics conjugated with the first pinhole mask. A grating is inserted into the beam upstream of the test optics and functions as a beam splitter in a typical interferometer. Thereafter, the beam is divided into high-order diffracted beams with small angular separation. The window transmits the first-order beam containing aberrations caused by the test optics and grating, and the pinhole, which is smaller than the diffraction-limited focus of the tested optics, diffracts the zeroth-order beam and generates a spherical wavefront that is used as a reference wavefront for interferometry. The two wavefronts produce interference fringe patterns, and the fringes can be detected by a CCD camera and analyzed to obtain the aberration information of the test optics.

EUV interferometry is also performed with LSI using a cross-grating beam splitter and applying a Fourier transform phase retrieval algorithm. This approach has been demonstrated to produce results consistent with the PDI to ~0.3–0.5 nm rms [2,3]. Other configurations of the LSI featuring double gratings [4] or a cross-grating setting in the Talbot plane [5–7] have been proposed as well. Basically, lateral shearing interferometry consists of displacing the defective wavefront laterally by a small amount and obtaining the interference pattern between the original and the displaced test wavefronts. Figure 1(b) shows the schematic diagram of our LSI system. An aberration-free spherical wavefront is generated by diffraction at the first pinhole placed in the object plane just as in the PDI. After passing through the test optics, the wavefront is diffracted by a linear binary grating or a cross grating. An order-selection mask that has two or four large windows is placed at the image plane. The window mask is set for blocking the undesired diffraction orders and selecting the test beams, in this case the ±1st orders. By using the order-selection mask for spatial filtering, optical noise is reduced and measurement precision is improved. The ±1st-order diffracted waves, which carry the aberration information of the test optics, interfere with each other. The interference fringe pattern can be detected with a CCD camera. To reconstruct the
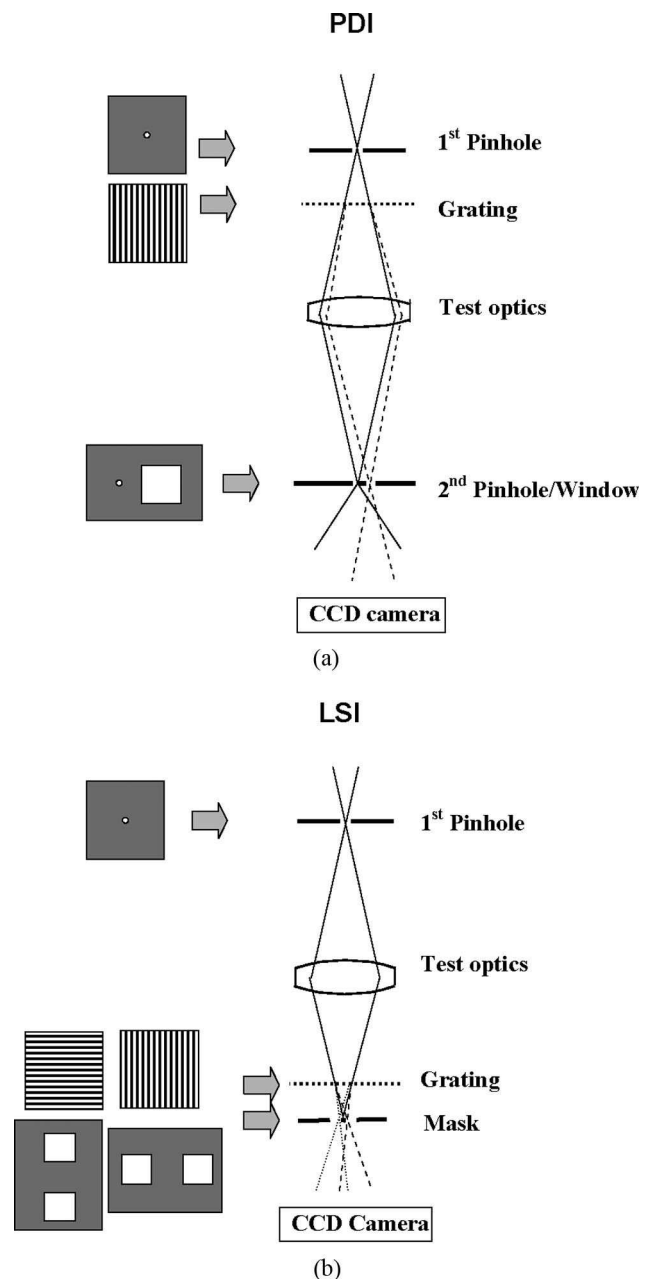

Fig. 1. Configurations of our experimental systems. (a) PDI: The second window transmits the first-order beam containing aberrations caused by the test optics and the second pinhole diffracts the zeroth-order beam and generates a spherical wavefront, which is used as a reference wavefront in the PDI. (b) LSI: The two windows on the mask transmit ±1st-order diffracted waves. Both of them carry the aberration information of the test optics but laterally shifted by a small amount. The original and the displaced test wavefronts produced the interference pattern in lateral shearing interferometry.

wavefront of the test optics, two sheared wavefronts normally in the orthogonal shear directions are required. The larger shearing amount is preferred to achieve higher measurement accuracy, while at the same time, the smaller grating pitch and the smaller space distance between the mask and grating are demanded. Phase analysis is carried out with a

phase-shifting method or Fourier transform phase retrieval.

3. Calibration Method for the Point Diffractive Interferometer

In the PDI configuration, the interferograms carry not only the phase differences between the test wavefront and reference wavefront but also the systematic aberration errors in the interferometer. Factors that determine the accuracy of the PDI include hyperbolic fringes (geometric coma), grating diffraction (coma), CCD camera-plane tilt and grating tilt, etc. [8]. Figure 2 illustrates the calibration measurement principle we proposed for the PDI. To achieve better fringe contrast, the zeroth-order beam focuses on the pinhole and the first-order beam of the test wavefront passes through the window; therefore the tested wavefront is a combined result of the test projection optics aberration and the grating diffraction aberration error, which only occurs in the diffracted beams. To extract the true wavefront of the test projection optics from the tested wavefronts, two measurements are needed. One measurement is carried out using the regular PDI configuration with a pinhole–window mask, and the other measurement is carried out with a window–window mask under the same diffraction order of the grating. Subtracting one measurement
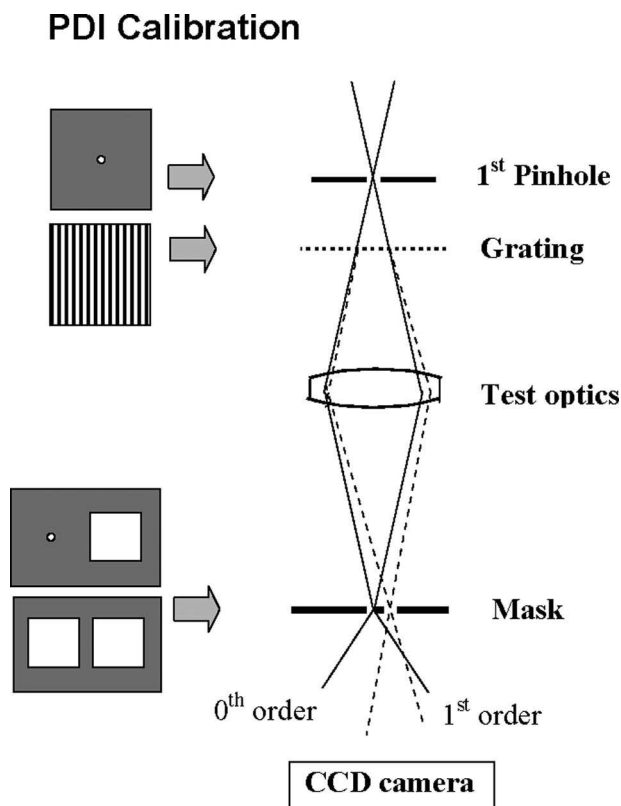
PDI Calibration

Fig. 2. Illustration of the calibration principle for the PDI: Two measurements were carried out by using two different mask patterns. Subtracting one measurement from the other, the result is the direct comparison between the wavefront aberration of the test optics and the ideal wavefront diffracted from the small pinhole.

from the other, the resulting wavefront is a direct comparison between the wavefront aberration of the projection optics and the reference wavefront diffracted from the second small pinhole. In a way, one can think of this as using an aberrated reference in the interferometer.

As a further explanation, assuming measurement T_1, taken with a pinhole–window mask, is described by

$$T_1 = (W_{T1} + W_{R1}) + W_{SYS1} - W_{R0}, \tag{1}$$

where W_{T1} is the real aberration of the test optics, deviated from an ideal spherical wavefront W_{R1}, that passes through the first-order window. W_{R0} is the zeroth-order diffraction-limited ideal reference spherical wavefront diffracted from the second pinhole of the PDI in Fig. 1(a). $W_{R1} - W_{R0}$ is the geometric optical path difference due to the two decentered nonaberrated spherical wavefronts, which produce the hyperbolic fringes that were analyzed to produce a systematic error in the PDI as tilts and comas. W_{SYS1} are the PDI systematic aberration errors, mainly including the diffraction error due to first-order diffraction of the grating and the positioning error of the fringe image detector, etc. If directly taking T_1 as the measured aberration of the test optics, the measurement accuracy is heavily dependent on the amount of the PDI systematic errors W_{SYS1}, whereas $W_{R1} - W_{R0}$ can be removed based on calculation. To improve the measurement accuracy by removing the PDI systematic errors W_{SYS1}, here we propose a method by taking a second measurement T_2 with a window–window mask as shown in Fig. 2 that can be described as

$$T_2 = (W_{T1} + W_{R1}) + W_{SYS1} - (W_{T0} + W_{R0}), \tag{2}$$

where W_{T0} is also the real aberration of the test optics but passes through the zeroth-order window instead of through the second pinhole in the first measurement as described in Eq. (1). Subtracting the two measurements of Eqs. (1) and (2), the difference between these two measurements is the real aberration of the test optics, i.e.,

$$W_3 = T_1 - T_2 = W_{T0}. \tag{3}$$

Therefore using the obtained W_3 as the final measurement instead of T_1 in the conventional PDI could improve the absolute measurement accuracy since the systematic error W_{SYS1} in Eq. (1) has been removed. Furthermore, numerically shifting W_3 in the amount of Δ corresponding to the zeroth- and first-order diffraction beam separation in the image, Eq. (3) becomes

$$W_{3\to\Delta} = W_{T0\to1} = W_{T1}. \tag{4}$$

Then subtracting Eq. (4) from the PDI measurement of Eq. (1), we obtain

$$W_4 = T_1 - W_{3 \to \Delta} = W_{SYS1} + (W_{R1} - W_{R0}). \qquad (5)$$

W_4 gives the total systematic errors, including the grating diffraction error, which exits only in the diffraction order, the geometric aberration caused by laterally shifting two ideal spherical wavefronts, and the positioning error of the fringe image detector effects. The precondition of this calibration method assumes the PDI produces the ideal spherical wavefront from both the first and second pinholes. The calibration accuracy could be affected by the variations of environment and the small systematic error deviations between the two measurements of Eqs. (1) and (2).

4. Phase-Shifting Algorithm Series for the Lateral Shearing Interferometer

In the LSI, to address the problem of undesired diffraction interference of 0th and higher orders, although the even orders are suppressed by choice of a duty ratio of 50% and a sideband filter, placed at the focal plane of the optics to select the wanted $\pm$1st order beam and stop the undesired 0th and higher diffraction orders, a certain percentage of the 0th order beam leaks through the $\pm$1st-order window (Fig. 3) and that can reduce the measurement accuracy. To solve this problem, we propose using the general approach [9,10] to derive a phase-shift algorithm series that can suppress the zeroth-order effect. We express the actual phase in a convenient form that takes the errors into account and develop the detected phase from a generic algorithm. Setting to zero the terms that involve unwanted errors leads to a set of algorithm coefficients, which can thus be found. By using this approach, one could develop an algorithm series for an individual interferometer based on relevant concerns about the main error sources and eliminate the error source effects to any desired order.

Here we express a three-beam interferometer, i.e., two signal beams and one noise beam. The central task is to estimate the interference phase of the signal without the effect of the noise beam. In the Fig. 1(b) LSI setup, the three interfering wavefronts are the -1st order, $E_{-1} = a_{-1} \exp(kW_{-1})$; the 0th order, $E_0 = a_0 \exp(kW_0)$; and the 1st order, $E_1 = a_1 \exp(kW_1)$, of the grating, where a_{-1}, a_0, a_1 and W_{-1}, W_0, W_1 are amplitudes and phases of the -1st, 0th, and 1st orders of the diffraction wavefronts. The interference fringe intensity of the three wavefronts are expressed as
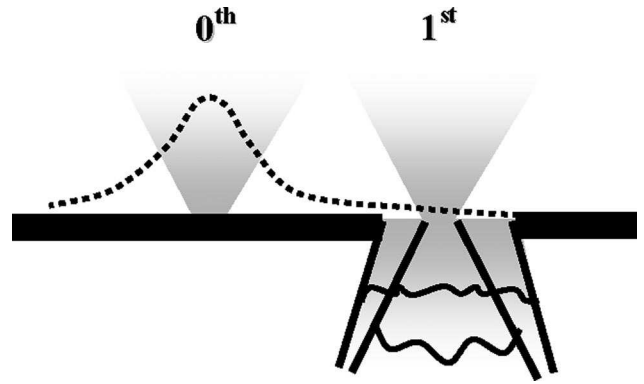

Fig. 3. Illustrating that, although the order-selective window is designed to only pass the test beam, i.e., the 1st- (or the -1st-) order diffraction beam, the 0th-order noise beam could spread and pass through the order-selective window, too; therefore it interferes with the test beam and as a result it reduces the measurement accuracy.

$$\begin{aligned}
g_0 = {} & a_0{}^2 + a_1{}^2 + a_{-1}{}^2 + 2a_0 a_1 \cos[k(W_1 - W_0)] \\
& + 2a_0 a_{-1} \cos[k(W_0 - W_{-1})] \\
& + 2a_1 a_{-1} \cos[k(W_1 - W_{-1})], \qquad (6)
\end{aligned}$$

where $W_1 - W_{-1}$ expresses the shear wavefront, which is to be tested, and $W_1 - W_0$ and $W_0 - W_{-1}$ are noise due to the unwanted zeroth-order beam. Assuming the grating displacement is Δx and the grating pitch is p, the phase-shift amount $\Delta\phi$ follows the function

$$\Delta\phi = 2\pi m \Delta x / p, \qquad (7)$$

where m is the diffraction order of the wavefront. Therefore taking the undesired zeroth-order into account, we have

$$(g_3 - g_{-3}) - (g_1 - g_{-1}) = 8a_1 a_{-1} \sin[k(W_1 - W_{-1})], \qquad (8)$$

$$(g_4 + g_{-4})/2 - (g_2 + g_{-2}) + g_0 = 8a_1 a_{-1} \cos[k(W_1 - W_{-1})], \qquad (9)$$

which are free from the zeroth-order wavefront, where $g_{-4}, g_{-3}, \ldots, g_0, \ldots, g_3, g_4$ are fringe intensities with $\pi/2$ phase shifts between W_1 and W_{-1}. Therefore, the detected phase with the nine-frame algorithm from Eqs. (8) and (9) is

$$k(W_1 - W_{-1}) = \tan^{-1}\left[\frac{2(g_3 - g_{-3}) - 2(g_1 - g_{-1})}{(g_4 + g_{-4}) - 2(g_2 + g_{-2}) + 2g_0}\right]. \qquad (10)$$

The phase-shifting algorithm that immunizes the zeroth-order noise beam effect generally takes the form

$$k(W_1 - W_{-1}) = \tan^{-1}\left[\frac{\sum_{m=0}^{N}\left[2(g_{4m+3} - g_{-(4m+3)}) - 2(g_{4m+1} - g_{-(4m+1)})\right]}{\sum_{m=0}^{N}\left[(g_{4m+4} + g_{-(4m+4)}) - 2(g_{4m+2} + g_{-(4m+2)}) + (g_{4m} + g_{-4m})\right]}\right], \qquad (11)$$

where m and N are integers.

5. Experimental Setup

The NewSUBARU synchrotron facility at the University of Hyogo is an electron storage ring, the electron energy of which is 1 GeV. The long undulator (LU) is inserted into one of the straight sections and is 10.8 m long. The periodic length of the LU magnetic field is 5.4 cm, and the periodic number is 200. The so-called K factor of the LU is set to be ~1.3 to yield the 13 nm radiation. This way, the LU was optimized to yield strong radiation near 13 nm. To select the best suitable conditions to evaluate the wavefront quality of the optical projection lens at the manufacturing level, we have built an EUV experimental measurement interferometer (EEI) (Fig. 4) using Schwarzschild-type test optics and installed the system in the NewSUBARU beam line of the LU. The beam coming from the undulator is focused on the first pinhole mask placed at the object plane of the test optic by a Schwarzschild-type illuminator. The EEI has five piezostages for precise alignment of optical components such as pinhole masks and gratings. Each mask and grating contains many different patterns and gratings. We can easily change the type of testing interferometer by exchanging patterns on these masks and gratings. The test optics was designed to have a demagnification of 20× and an image-side numerical aperture of 0.2. The mirror surfaces were coated with Mo–Si multilayers.

In the PDI, a beam-splitter grating was placed upstream of the optics, following the configuration shown schematically in Fig. 1(a). The PDI uses a small pinhole on the first mask and an aberration-free spherical wavefront is generated by the pinhole. The spherical wavefront is divided into the 0th- and ±1st-order diffracted waves by a binary grating. These waves pass through the test optics and arrive at a second pinhole mask, which has a small pinhole and a large window. The zeroth-order wave passes through the small pinhole and generates a spherical wave again. One of the first-order diffracted waves goes through the large window, carrying the aberration information of the test optics. These two waves interfere and the interference fringes are observed by a CCD camera. In the calibrated PDI, illustrated in Fig. 2, proposed in this paper, the mask pattern containing two large windows was also included. The absolute PDI uses two measurements. The first measurement is carried out using the standard PDI configuration with a pinhole–window mask. The second measurement is carried out with a window–window
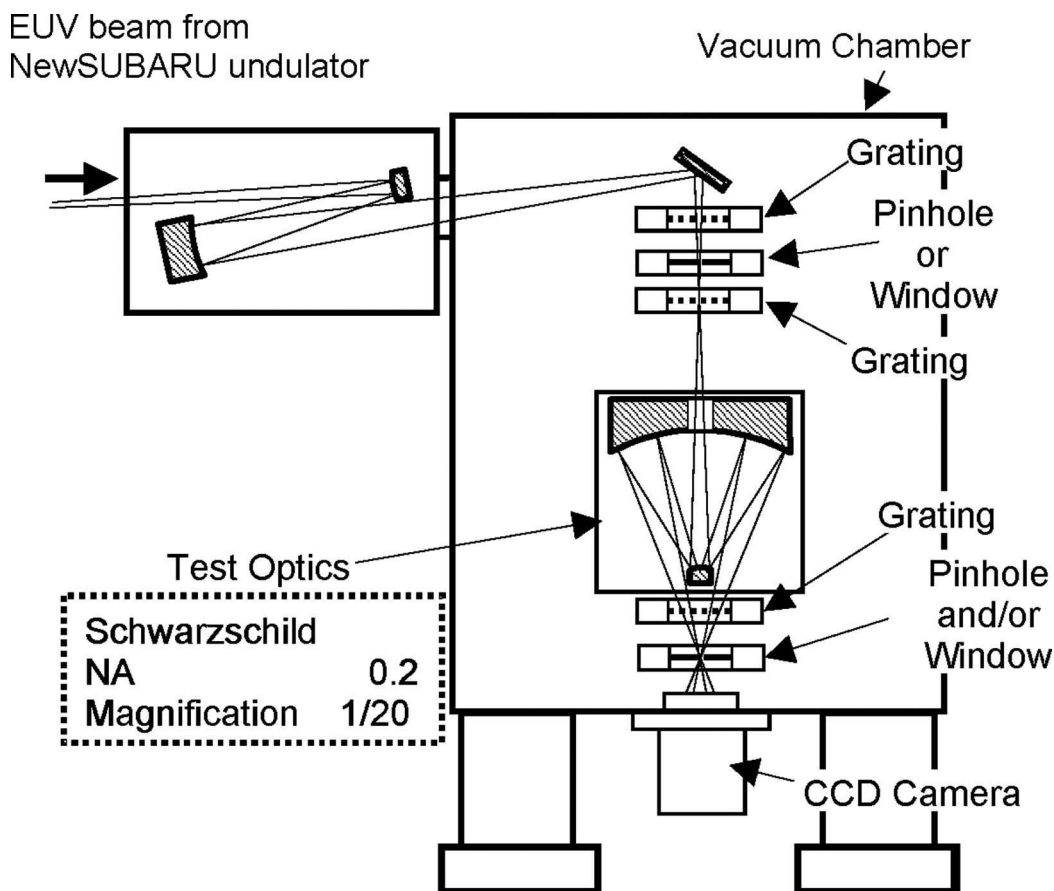

Fig. 4. Experimental setup: The beam coming from the undulator is focused on the first pinhole mask placed at the object plane of the test optic by a Schwarzschild-type illuminator. The EEI has five piezostages for precise alignment of optical components such as pinhole masks and gratings. Each mask and grating contains many different patterns and gratings for the different types of interferometer.

mask under the same diffraction orders of the grating. The second measurement is used as calibration data of the systematic error of the interferometer. Only the first-order beam includes the diffraction aberrations. Both measurements have the same systematic errors. According to Eqs. (1)–(3), subtracting one measurement from the other, the result is a direct comparison between the wavefront aberration of the test optics and the ideal wavefront diffracted from the small pinhole.

The LSI, illustrated in Fig. 1(b), was realized by placing a grating beam splitter downstream of the optics and the mask was chosen to contain two large windows in the image plane so as to transmit the ±1st orders. When the initial pinhole is illuminated by the EUV radiation, an aberration-free spherical wavefront is generated by diffraction at the first pinhole. The aberration-free wave goes through the test optics. The wave passing through the optics is aberrated and diffracted by a binary grating. An order-selection mask is placed at the image plane of the optics under test. The mask has two large windows that act as a spatial filter. Only the ±1st-order diffracted waves can pass through the windows and 0th and higher order diffracted waves are blocked by the order-selection mask. By using the order-selection mask for spatial filtering, noise is reduced and measurement precision is improved. The ±1st-order diffracted waves, which carry the aberration information of the test optics, interfere with each other and the fringe patterns are detected with the same CCD camera as for the PDI.
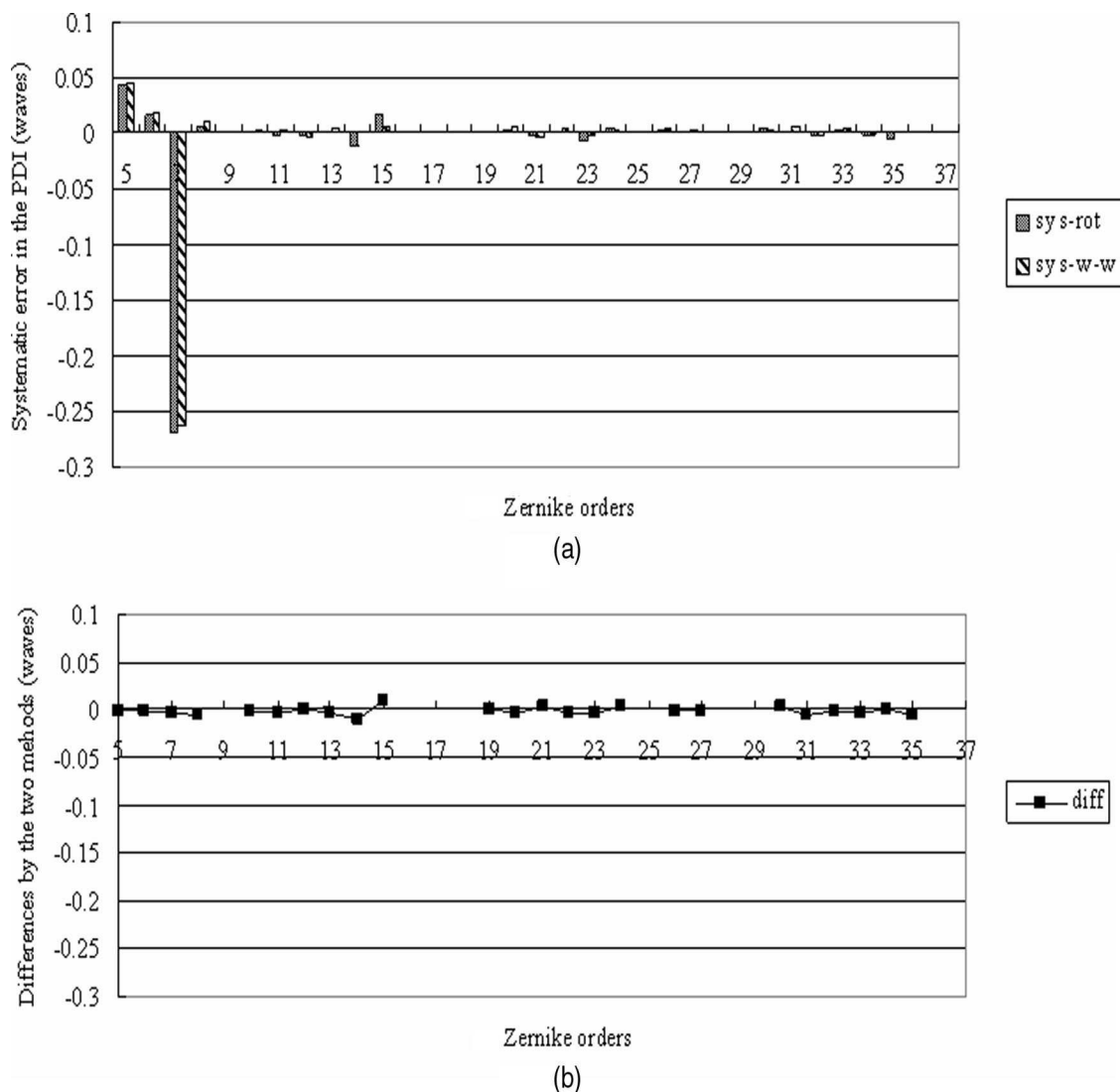

Fig. 5. Comparisons between two different calibration methods: The agreement between these two different methods confirmed our proposed calibration principle experimentally as the rotation method is generally considered one with high accuracy and reliability. The 9th, 16th, and 25th Zernike orders are not compared due to their axial symmetry. The 17th, 18th, 28th, and 29th orders are not compared due to the choice of rotation angle of 90°. (a) Systematic aberration errors expressed in Zernike polynomials measured by the two different calibration methods (sys-rot: obtained by the rotation method; sys-w-w: obtained by the proposed method in this paper). (b) Differences between the systematic errors in the PDI measured by these two different calibration methods.

6. Proof-of-Principle Experiments

A. Calibration Method for the Point Diffractive Interferometer

To experimentally assess the calibration accuracy of our proposed method in Section 3, on the one hand, following the measurement principle illustrated in Fig. 2, we took two measurements with the window–pinhole mask and the window–window mask on an EEI, respectively, and calculated the total systematic aberration of the PDI with Eq. (5). On the other hand, we used one other conventional calibration method and measured the same Schwarzschild-type projection optics in two different orientations of the test optics, by rotating the test optics axially 90° while the systematic errors were kept unchanged as follows:

$$T_2^R = (W_{T1}^R + W_{R1}) + W_{SYS1} - W_{R0}, \quad (12)$$

where T_2^R is the tested wavefront after the tested optics is rotated 90°. W_{T1}^R denotes the wavefront of the tested optics after it is rotated. By further rotating the tested wavefront numerically back in the opposite direction from Eq. (12),

$$W_5 = (W_{T1} + W_{R1}^{-R}) + W_{SYS1}^{-R} - W_{R0}^{-R} \quad (13)$$

was obtained. By subtracting measurement Eq. (13) from measurement Eq. (1), we have

$$T_1 - W_5 = (W_{SYS1} - W_{SYS1}^{-R}) + (W_{R1} - W_{R0}) - (W_{R1}^{-R} - W_{R0}^{-R}). \quad (14)$$

The tested wavefront is used to expand into a set of basic orthogonal functions. For the ring field such as that produced by a Schwarzschild optical system,
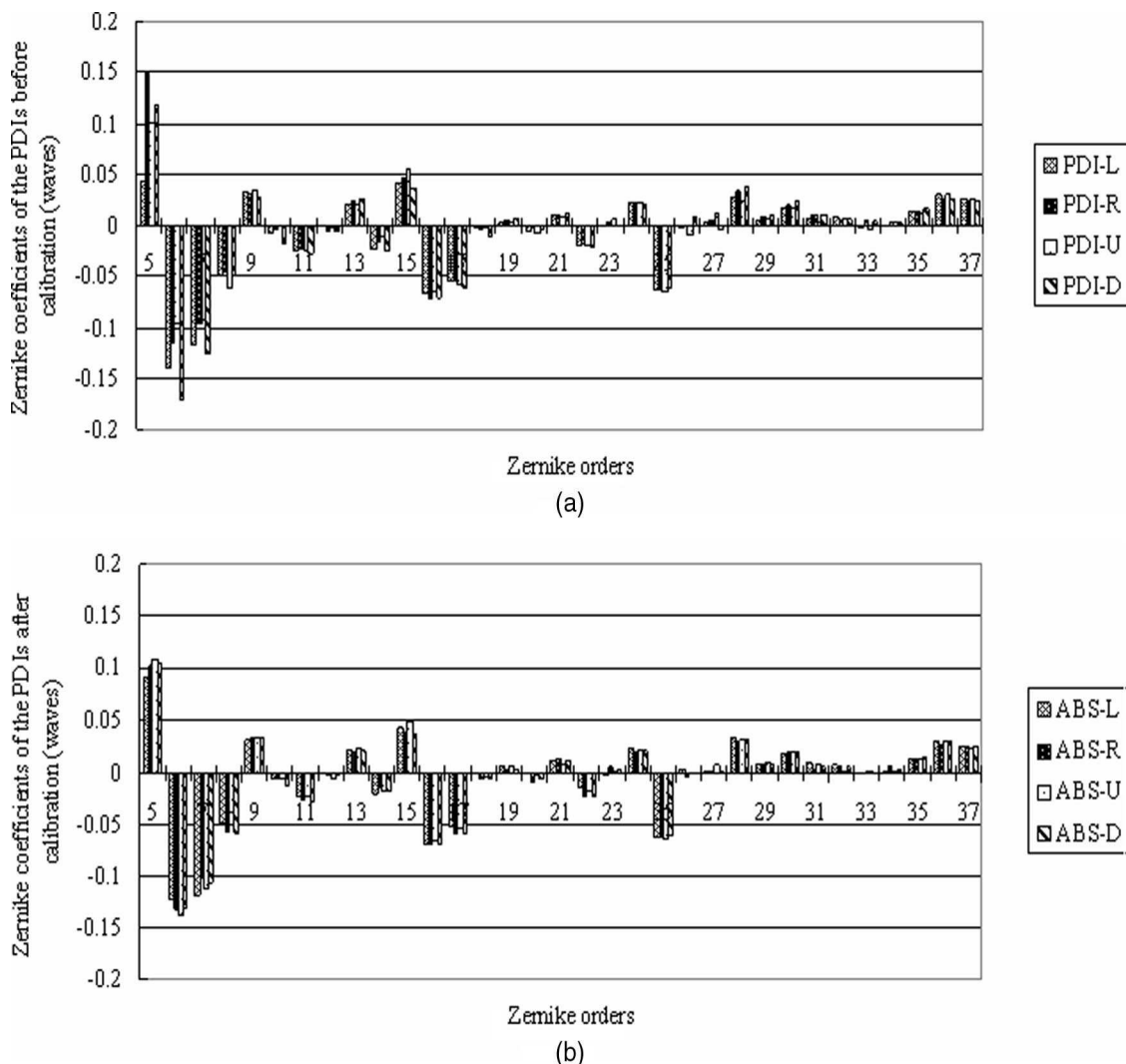

Fig. 6. Larger deviations among the measurements before calibration are considered mainly due to the different systematic errors in the different PDI structure. The consistency in the results after employing our proposed calibration method indicates the achievable calibration accuracy experimentally. (a) Measured wavefronts on an EEI based on the configuration of the Fig. 1(a) PDI before calibration. (b) Measured wavefronts on an EEI based on the configuration of the Fig. 2 PDI after calibration.

these expansion functions are annular Zernike polynomials. The optimal coefficients are determined based on the least-squares fitting method. From the two measurements before and after the optics was rotated, one can only obtain the axially asymmetric components of the total systematic aberration:

$$W_6 = W_{SYS1} + (W_{R1} - W_{R0}). \tag{15}$$

We finally obtained the annular Zernike polynomial coefficients of the systematic aberration from these two methods based on Eqs. (5) and (14) and plotted them in Fig. 5, noted as sys-w-w for our proposed method and sys-rot for the other rotation method. Although the calibration method proposed in Section 3 is also able to detect the axially symmetrical components, only the axially asymmetrical components of the systematic aberration are shown in Fig. 5 for comparison. As a result, we reconstruct the obtained systematic error wavefront with the calculated coefficients shown in Fig. 5(a) and the corresponding annular Zernike polynomials; the systematic aberration wavefront of the PDI had a rms value of 1.31 nm from our proposed calibration method and 1.29 nm rms from the rotation calibration method. Taking the

differences of these two measured sets of annular Zernike coefficients as shown in Fig. 5(b) and in the same way above, we reconstruct the wavefront difference between these two methods; the rms value of the wavefront differences was 0.086 nm. The agreement between these two different methods proved our proposed calibration principle experimentally and also indicated the achievable high accuracy of our proposed calibration method for the PDI, by comparison with the rotation method as it is generally considered one with high accuracy and reliability.

Figure 6 shows measured results based on the PDI setup but with four different arrangements. PDI-R is with the pinhole on the right side of the window, whereas PDI-L is on the left. PDI-U and PDI-D are with the pinholes on the upside and downside, respectively. Each PDI used a different diffraction pinhole as a reference. PDI-R and PDI-L used the same grating, whereas PDI-U and PDI-D shared another orthogonal grating. The maximum deviation to the averaged measurement aberration wavefront of the four PDIs is ~0.35 nm rms before calibration [Fig. 6(a)]. But after taking second measurements with two large windows following Fig. 2 and subtracting the systematic aberration errors
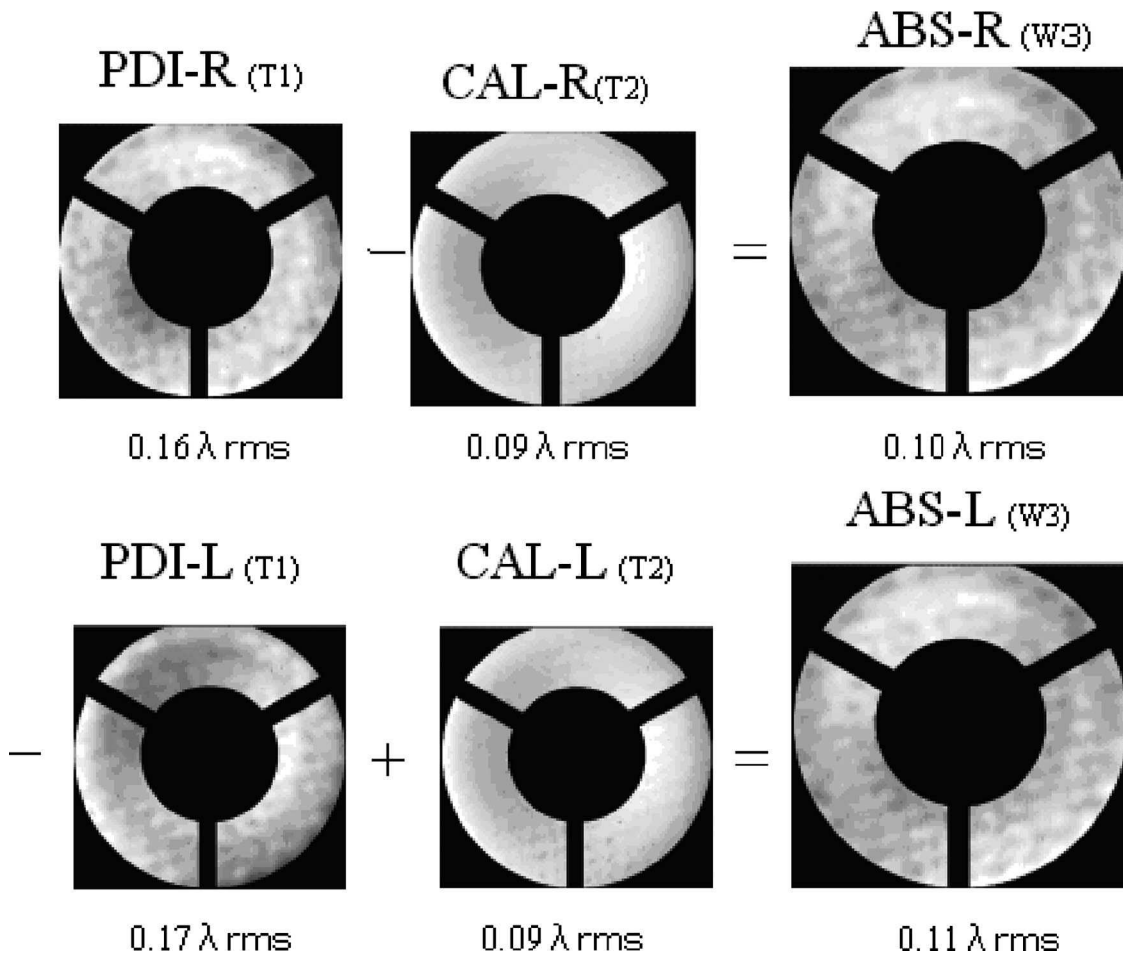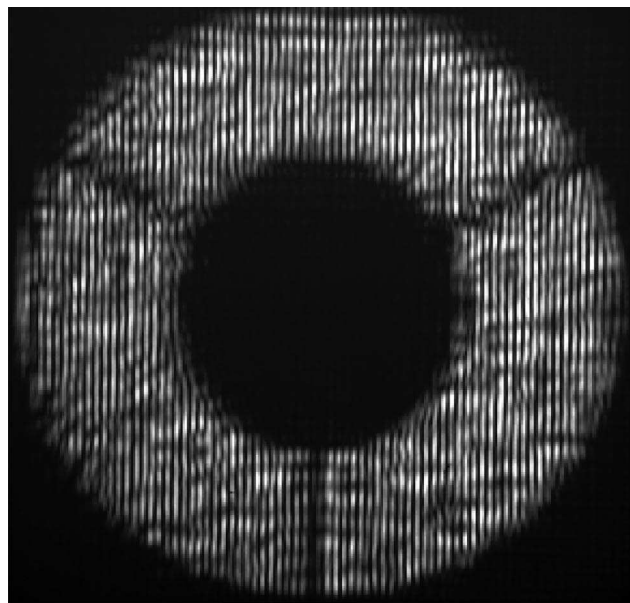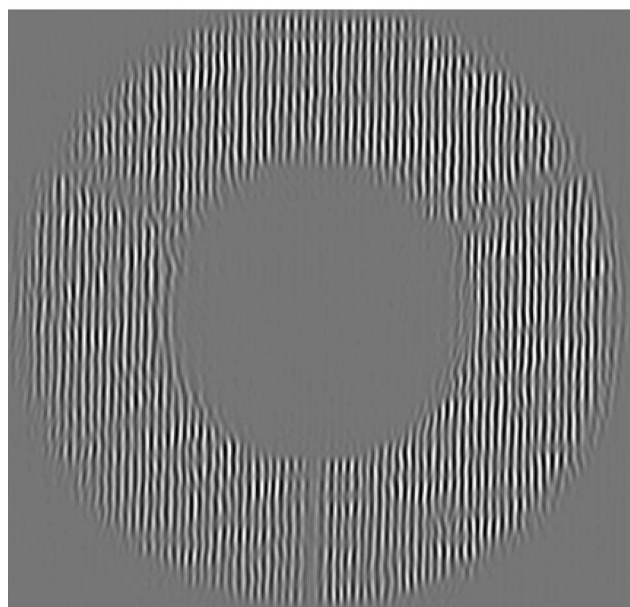

Fig. 7. Measured wavefronts on an EEI to illustrate the principle of the calibration method described in Section 3. Some of the wavefronts expressed in Zernike coefficients have appeared in Figs. 6(a) and 6(b).

from them respectively as indicated with Eq. (3), the measurement results from these calibrated PDIs attained consistency within 0.14 nm rms [Fig. 6(b)]. The larger differences among the measurements before calibration are considered mainly due to the different systematic errors in the different PDI structure. The consistency in the results after employing our proposed calibration method indicates the achievable calibration accuracy experimentally. The main remaining errors could be due to the reference wavefront defects in the PDIs. Figure 7 illustrates the calibration procedure by measuring the wavefront of the test Schwarzschild-type projection optics on the PDI-R and PDI-L following Eqs. (1)–(3) experimentally.

B. Phase Analysis Algorithm Series for the Lateral Shearing Interferometer

To experimentally confirm the zeroth-order noise-beam-insensitive property of the phase analysis algorithm of Eq. (10), we took two sets of measurements of nine frames with $\pi/2$ phase shifts using the LSI mode on an EEI, as shown in Fig. 1(b). The unwanted zeroth-order beam remained in the set 1 interferograms [one example shown in Fig. 8(a)] and was partially removed by the Fourier transform method for comparison in the set 2 interferograms [one example in Fig. 8(b)]. For comparison, we selected the nine-frame phase-shifting algorithm described by Eq. (16), which was not derived from removing the zeroth noise beam [9]:

$$k(W_1 - W_{-1}) = \tan^{-1}\left[\frac{26(g_1 - g_{-1}) - 6(g_3 - g_{-3})}{16(g_2 + g_{-2}) - (g_4 + g_{-4}) - 30g_0}\right].$$
(16)

The derivation process of the phase-shift analysis algorithms described in Section 4 indicated that the zeroth-order beam would not affect the measurement accuracy when Eq. (10) is applied, whereas Eq. (16) was not designed for this purpose. In this experiment, those two sets of interferograms with and without a zeroth-order beam in the interferograms were analyzed with Eqs. (10) and (16), respectively. For each algorithm, the differences between these two analyzed results are expressed with 37 annular Zernike polynomials and plotted in Fig. 9. In the case of using

(a)

(b)

Fig. 8. Measured interferometric fringes of the LSI on an EEI used in the comparisons of different algorithms to verify that Eq. (10) itself is sufficient to eliminate the zeroth-order beam effect as its principle implied. (a) Example of the measured fringe of the LSI [Fig. 1(b)] with the zeroth-order noise beam effect remaining. (b) Example of the measured fringe of the LSI where the zeroth-order noise beam was partially removed by the Fourier transform method for comparison.
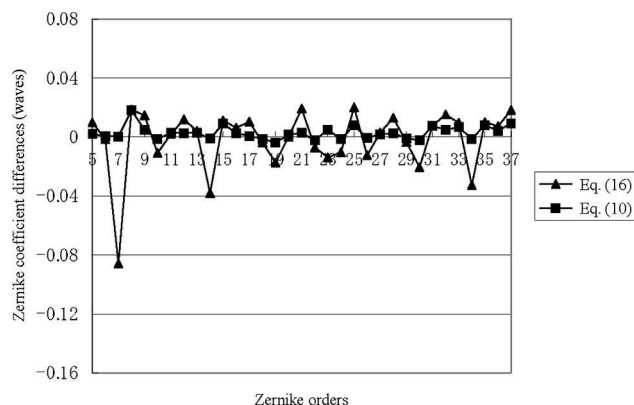

Fig. 9. Measured wavefront differences obtained from two sets of interferograms shown in Figs. 8(a) and 8(b) using Eqs. (10) and (16), respectively. The difference when Eq. (10) was applied was much smaller than the case when Eq. (16) was applied. It experimentally indicated that the measurement accuracy was less affected by the zeroth-order noise beam when Eq. (10) was applied.

Eq. (10), the difference is much smaller than in the case of applying Eq. (16). This indicated experimentally that the measurement accuracy was less effected by the zeroth-order noise beam when Eq. (10) was applied. This measurement result showed experimentally that Eq. (10) itself is sufficient to eliminate the zeroth-order beam effect as its principle implied.

7. Summary

We have described our configurations of the point diffraction interferometer and the lateral shearing interferometer for characterizing the projection lithography optics at the operational wavelength employed in EUVL. A simple but easy-to-perform calibration method for the PDI was proposed. A zeroth-order noise-beam-insensitive phase-shifting algorithm series was proposed for the LSI. Some experimental results were presented that show self-approved consistency of the calibration method and the algorithm series we proposed.

References

1. K. A. Goldberg, P. Naulleau, S. H. Lee, C. Chang, C. Bresloff, R. Gaughan, H. N. Chapman, J. Goldsmith, and J. Bokor, "Direct comparison of EUV and visible-light interferometries," Proc. SPIE **3676,** 635–642 (1999).
2. K. A. Goldberg, P. Naulleau, P. Denham, S. B. Rekawa, K. Jackson, J. A. Liddle, and E. H. Anderson, "EUV interferometric testing and alignment of the 0.3 NA MET optic," Proc. SPIE **5374,** 64–73 (2004).
3. S. Kato, C. Ouchi, M. Hasegawa, A. Suzuki, T. Hasegawa, K. Sugisaki, M. Okada, Y. Zhu, K. Murakami, J. Saito, M. Niibe, and M. Takeda, "Comparison of EUV interferometry methods in EUVA project," Proc. SPIE **5751,** 110–117 (2005).
4. Z. Liu, K. Sugisaki, Y. Zhu, M. Ishii, K. Murakami, J. Saito, A. Suzuki, and M. Hasegawa, "Double-grating lateral shearing interferometer for extreme ultraviolet lithography," Jpn. J. Appl. Phys. **43,** 3718–3721 (2004).
5. M. Takeda and S. Kobayashi, "Lateral aberration measurements with a digital Talbot interferometer," Appl. Opt. **23,** 1760–1764 (1984).
6. P. P. Naulleau, K. A. Goldberg, and J. Bokor, "Extreme ultraviolet carrier-frequency shearing interferometry of a lithographic four-mirror optical system," J. Vacuum Sci. Technol. B **18,** 2939–2943 (2000).
7. M. Hasegawa, C. Ouchi, T. Hasegawa, S. Kato, A. Ohkubo, A. Suzuki, K. Sugisaki, M. Okada, K. Otaki, K. Murakami, J. Saito, M. Niibe, and M. Takeda, "Recent progress of EUV wavefront metrology in EUVA," Proc. SPIE **5533,** 27–36 (2004).
8. K. A. Goldberg, "EUV interferometry," Ph.D. dissertation (Univ. of California, Berkeley, 1997).
9. Y. Zhu and T. Gemma, "Method for designing error-compensating phase-calculation algorithms for phase-shifting interferometry," Appl. Opt. **40,** 4540–4546 (2001).
10. Y. Zhu, K. Sugisaki, K. Murakami, K. Ota, H. Kondo, M. Ishii, J. Kawakami, T. Oshino, J. Saito, A. Suzuki, M. Hasegawa, Y. Sekine, S. Takeuchi, C. Ouchi, O. Kakuchi, and Y. Watanabe, "Shearing interferometry for at wavelength wavefront measurement of extreme-ultraviolet lithography projection optics," Jpn. J. Appl. Phys. Part 1 **42,** 5844–5847 (2003).